
Reciprocal Adversarial Learning via Characteristic Functions

Shengxi Li* Zeyang Yu Min Xiang Danilo Mandic
 Imperial College London
 {shengxi.li17, z.yu17, m.xiang13, d.mandic}@imperial.ac.uk

Abstract

Generative adversarial nets (GANs) have become a preferred tool for tasks involving complicated distributions. To stabilise the training and reduce the mode collapse of GANs, one of their main variants employs the integral probability metric (IPM) as the loss function. This provides extensive IPM-GANs with theoretical support for basically comparing moments in an embedded domain of the *critic*. We generalise this by comparing the distributions rather than their moments via a powerful tool, i.e., the characteristic function (CF), which uniquely and universally comprises all the information about a distribution. For rigour, we first establish the physical meaning of the phase and amplitude in CF, and show that this provides a feasible way of balancing the accuracy and diversity of generation. We then develop an efficient sampling strategy to calculate the CFs. Within this framework, we further prove an equivalence between the embedded and data domains when a reciprocal exists, where we naturally develop the GAN in an auto-encoder structure, in a way of comparing everything in the embedded space (a semantically meaningful manifold). This efficient structure uses only two modules, together with a simple training strategy, to achieve bi-directionally generating clear images, which is referred to as the reciprocal CF GAN (RCF-GAN). Experimental results demonstrate the superior performances of the proposed RCF-GAN in terms of both generation and reconstruction.

1 Introduction

Generative adversarial nets (GANs) owe their success to their powerful capability in capturing complicated data distributions [1]. In practical applications, however, their significant potential still remains under-explored as GANs typically suffer from unstable training and mode collapse issues [2]. An effective yet elegant way to address these issues is to replace the Jensen-Shannon (JS) divergence in measuring the discrepancy in the original form of GANs [3] by another class of metrics called the integral probability metric (IPM) [4] given by,

$$d(\mathcal{P}_d, \mathcal{P}_g) = \sup_{f \in \mathcal{F}} |\mathbb{E}_{x \sim \mathcal{P}_d}[f(x)] - \mathbb{E}_{x \sim \mathcal{P}_g}[f(x)]|, \quad (1)$$

where the symbol \mathcal{F} in IPMs represents a collection of (typically real) bounded functions, \mathcal{P}_g denotes the generated distribution, and \mathcal{P}_d is the real data distribution. Using IPMs to improve GANs has been justified by the fact that in real-world data distributions are typically embedded in low-dimensional manifolds, which is intuitive because data preserve semantic information instead of being a collection of rather random pixels. Thus, the divergence measure (“bin-to-bin” comparison) of the original GAN could easily max out, whereas the IPMs such as the Wasserstein distance (“cross-bin” comparison) can consistently yield a meaningful measure between the generated and real data distributions [3].

*Corresponding author

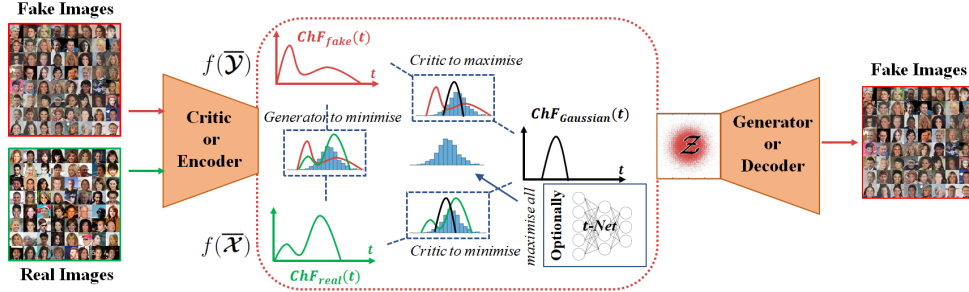


Figure 1: The overall structure of the proposed RCF-GAN. The generator serves to minimise the CF loss between the embedded real and fake distributions. The *critic* serves to minimise the CF loss between the embedded real and the input noise distributions, whilst maximising the CF loss between the embedded fake and the input noise distributions. Moreover, an MSE loss between the embedded fake and the input noise distributions is regularised as the auto-encoder loss, which has not been shown in the figure. An optional *t*-net can be employed to optimally sample the CF loss.

Varying collections of \mathcal{F} in (1), therefore, defines different IPM-GANs and the supremum $\sup_{f \in \mathcal{F}}$ is then typically achieved by the discriminator net, or more formally, the *critic* in the IPM-GANs. The first IPM-GAN was motivated by the Wasserstein GAN (W-GAN) [5], where \mathcal{F} denotes all the 1-Lipschitz functions. However, it has been widely argued that the *critic* is not powerful enough to search within all the 1-Lipschitz function spaces, which leads to limited diversity of the generator due to an ill-posed equivalence measurement of \mathcal{P}_d and \mathcal{P}_g [6, 7]. Follow-up works have been proposed to improve the W-GAN by either enhancing it to satisfy the 1-Lipschitz condition (e.g., by gradient penalty [8] or spectral normalization [9]) or by employing *easy-to-implement* \mathcal{F} for the *critic*. The latter, by virtue of relaxing the *critic*, typically leads to a stringent comparison on the embedded feature domain, i.e., by matching higher-order moments instead of the mean matching in the W-GAN. This path includes many recent GANs which additionally consider the second-order moment (e.g., Fisher-GAN [10] and McGAN [11]), together with explicitly (e.g., Sphere GAN [12]) or implicitly (e.g., MMD-GAN [13, 14]) comparing higher-order moments. Furthermore, generalising (1) as moment matching problem has been justified as a natural and beneficial way to understand IPM-GANs [15–17]. This also compensates for the deficiency where the *critic* may not transform the data distributions into unimodal distributions, for example, the Gaussian distribution that is solely determined by the first- and second-order moments.

Moreover, it is more safe and elegant to compare the distributions because the equivalence in distributions ensures the equivalence in the moments; the inverse, however, does not necessarily hold. As a powerful tool of containing all the information relevant to a distribution, the *characteristic function* (CF) provides a universal way of comparing distributions, even when their probability density functions (pdfs) do not exist. The CF also has a one-to-one correspondence with the cumulative density function (cdf), which has also been verified to benefit the design of GANs [18]. Compared to the moment generating function (mgf) that has been reflected in the MMD-GAN [13], the CF is unique and universally existent. More importantly, the CF is automatically aligned at $\mathbf{0}$; this means that even a simple “bin-to-bin” comparison between CFs can consistently provide a meaningful measure and thus avoid gradient vanishing that appears in the original GAN [5]. On the other hand, the weak convergence property of CFs ensures that the convergence in the CF also indicates the convergence in the distributions.

In this paper, we propose a reciprocal CF GAN (RCF-GAN) as a natural generalisation of the existing IPM-GANs, with the overall structure shown in Fig. 1. It needs to be pointed out that incorporating the CF in a GAN is non-trivial because the CF is basically complex-valued and the comparison has to be performed on functions as well. To address these difficulties, we first demystify the role of CFs by finding that its phase is closely related to the distribution centre, whereas the amplitude dominates the distribution scale. This provides a feasible way of balancing the accuracy and diversity of generation. Then, as for the comparison over functions, we prove that other than in the whole space of CFs, sampling within a small ball around $\mathbf{0}$ of CFs is sufficient to compare two distributions, and also enables the proposed CF loss to be bounded and differentiable almost everywhere. We further optimise the sampling strategy by automatically adjusting sampling distributions under the umbrella of the *scale mixture of normals* [19].

Benefiting from our powerful CF design in comparing distributions, we propose to purely compare in the embedded domain and prove its equivalence to the counterpart in the data domain when a reciprocal theory between the generator and the *critic* holds. This motivates us to incorporate an auto-encoder structure to satisfy this theoretical requirement. In this way, the *critic* in our RCF-GAN is further relaxed and only focuses on learning a fruitful embedding. Furthermore, different from many existing adversarial works with auto-encoders incorporating at least three modules² [13, 14, 21–26], our RCF-GAN only requires two modules that already exist in a GAN; the *critic* is an encoder and the generator is a decoder as well, which is neat and reasonable as this comes without increasing computational complexity and complicated (unstable) training strategies, as well as without other requirements such as the Lipschitz continuity. More importantly, the framework of comparing everything in the embedded domain enables the CF-GAN to learn a semantic and meaningful latent space, and to also avoid the smoothing artefact that arises from the use of point-wise mean square error (MSE) employed in the data domain. This benefits from both the auto-encoder and the GANs, i.e., *bi-directionally* generating *clear* images. Our experimental results show that our RCF-GAN achieves remarkable improvements on the generation, together with an additional capability in the reconstruction and interpolation³.

2 Characteristic Function Loss and Efficient Sampling Strategy

2.1 Characteristic Function and Elliptical Distribution

The CF of a random variable, $\mathcal{X} \in \mathbb{R}^m$, represents the expectation of its complex unitary transform, given by

$$\Phi_{\mathcal{X}}(\mathbf{t}) = \mathbb{E}_{\mathcal{X}}[e^{j\mathbf{t}^T \mathbf{x}}] = \int_{\mathbf{x}} e^{j\mathbf{t}^T \mathbf{x}} dF_{\mathcal{X}}(\mathbf{x}), \quad (2)$$

where $F_{\mathcal{X}}(x)$ is the cdf of \mathcal{X} . We thus have $\Phi_{\mathcal{X}}(\mathbf{0}) = 1$ and $|\Phi_{\mathcal{X}}(\mathbf{t})| \leq 1$ for all \mathbf{t} . This property ensures that CFs can be straightforwardly compared in a “bin-to-bin” manner, because all CFs are automatically aligned at $\mathbf{t} = \mathbf{0}$. Moreover, when the pdf of \mathcal{X} exists, the expression in (2) is equal to its inverse Fourier transform; this ensures that $\Phi_{\mathcal{X}}(\mathbf{t})$ is uniformly continuous. Another important property of the CF is that it uniquely and universally retains all the information regarding a random variable. In other words, a random variable does not necessarily need to possess a pdf (e.g., when it is an α -stable distribution), but its CF always exists.

As the cdf, $F_{\mathcal{X}}(\mathbf{x})$, is unknown and is to be compared, we employ the empirical characteristic function (ECF) as an asymptotic approximation in the form of $\hat{\Phi}_{\mathcal{X}_n}(\mathbf{t}) = \sum_{i=1}^n e^{j\mathbf{t}^T \mathbf{x}_i}$, where $\{\mathbf{x}_i\}_{i=1}^n$ are n i.i.d. samples drawn from \mathcal{X} . As a result of the *Levy continuity theorem* [28], the ECF converges weakly to the population CF [29]. More importantly, the *uniqueness theorem* guarantees that two random variables have the same distribution if and only if their CFs are identical [30]. Therefore, together with the weak convergence, the ECF provides a feasible and good proxy to the distribution, which has also been preliminarily applied in two sample test [31, 32]. Before proceeding further, we introduce an important class of distributions that will be used in this work.

Example 1. *Within unimodal distributions, one broad class of distributions is called the elliptical distribution, which is general enough to include various important distributions such as the Gaussian, Laplace, Cauchy, Student-t, α -stable and logistic distributions. The elliptical distributions do not necessarily have pdfs, and we refer to [33] for more detail. The CF of an elliptical distribution, \mathcal{X} , however, always exists and has the following form*

$$\Phi_{\mathcal{X}}(\mathbf{t}) = e^{j\mathbf{t}^T \boldsymbol{\mu}} \psi(\mathbf{t}^T \boldsymbol{\Sigma} \mathbf{t}), \quad (3)$$

where $\boldsymbol{\mu}$ denotes the distribution centre, $\boldsymbol{\Sigma}$ is the distribution scale, and $\psi(\cdot)$ is a real-valued function $\mathbb{R} \rightarrow \mathbb{R}$, for example, $\psi(s) = e^{(-s/2)}$ for the Gaussian distribution. By inspecting (3) we can see that the phase of the CF is solely related to the location of data centre and the amplitude is only governed by the distribution scale (diversity).

²To our best knowledge, the only exception is the AGE [20], which adopts two modules in an auto-encoder under a max-min problem and different losses. Please see the *Related Works* for the difference.

³A very recent independent work [27] named OCF-GAN also employs the CF as a replacement by using the same structure of MMD-GANs. The proposed RCF-GAN is substantially different from that in [27]. We refer to the *Related Works* in the supplementary material for a detailed explanation.

2.2 Distance Measure via Characteristic Functions

The auto alignment property of the CFs allows us to incorporate a simple “bin-to-bin” comparison over two complex-valued CFs (corresponding to two random variables \mathcal{X} and \mathcal{Y}), in the form

$$\mathcal{C}_{\mathcal{T}}(\mathcal{X}, \mathcal{Y}) = \int_{\mathbf{t}} \underbrace{((\Phi_{\mathcal{X}}(\mathbf{t}) - \Phi_{\mathcal{Y}}(\mathbf{t}))(\Phi_{\mathcal{X}}^*(\mathbf{t}) - \Phi_{\mathcal{Y}}^*(\mathbf{t})))^{\frac{1}{2}}}_{c(\mathbf{t})} dF_{\mathcal{T}}(\mathbf{t}), \quad (4)$$

where Φ^* denotes the complex conjugate of Φ and $F_{\mathcal{T}}(\mathbf{t})$ is the cdf of a sampling distribution on \mathbf{t} . For the convenience of subsequent analysis, we represent the quadratic term for each \mathbf{t} as $c(\mathbf{t}) = (\Phi_{\mathcal{X}}(\mathbf{t}) - \Phi_{\mathcal{Y}}(\mathbf{t}))(\Phi_{\mathcal{X}}^*(\mathbf{t}) - \Phi_{\mathcal{Y}}^*(\mathbf{t}))$. More importantly, $\mathcal{C}_{\mathcal{T}}(\mathcal{X}, \mathcal{Y})$ is a valid distance that measures the difference of two random variables via CFs, of which the proof is provided in Lemma 1; this means $\mathcal{C}_{\mathcal{T}}(\mathcal{X}, \mathcal{Y}) = 0$ if and only if $\mathcal{X} =^d \mathcal{Y}$. A specific type of $\mathcal{C}_{\mathcal{T}}(\mathcal{X}, \mathcal{Y})$ in (4) is when the pdf of \mathbf{t} is proportional to $\|\mathbf{t}\|^{-1}$, and its relationship to other metrics, including the Wasserstein and Kolmogorov distances, has been analysed in detail [34].

Lemma 1. *The discrepancy between \mathcal{X} and \mathcal{Y} , given by $\mathcal{C}_{\mathcal{T}}(\mathcal{X}, \mathcal{Y})$ in (4), is a distance metric when the support of \mathcal{T} resides in \mathbb{R}^m .*

Furthermore, as the phase and amplitude of a CF indicate the data centre and diversity, we inspect $c(\mathbf{t})$ and rewrite it in a physically meaningful way, i.e., through the differences in the corresponding phase and amplitude terms as [35, 36],

$$\begin{aligned} c(\mathbf{t}) &= |\Phi_{\mathcal{X}}(\mathbf{t})|^2 + |\Phi_{\mathcal{Y}}(\mathbf{t})|^2 - \Phi_{\mathcal{X}}(\mathbf{t})\Phi_{\mathcal{Y}}^*(\mathbf{t}) - \Phi_{\mathcal{Y}}(\mathbf{t})\Phi_{\mathcal{X}}^*(\mathbf{t}) \\ &= |\Phi_{\mathcal{X}}(\mathbf{t})|^2 + |\Phi_{\mathcal{Y}}(\mathbf{t})|^2 - |\Phi_{\mathcal{X}}(\mathbf{t})||\Phi_{\mathcal{Y}}(\mathbf{t})|(2 \cos(\mathbf{a}_{\mathcal{X}}(\mathbf{t}) - \mathbf{a}_{\mathcal{Y}}(\mathbf{t}))) \\ &= |\Phi_{\mathcal{X}}(\mathbf{t})|^2 + |\Phi_{\mathcal{Y}}(\mathbf{t})|^2 - 2|\Phi_{\mathcal{X}}(\mathbf{t})||\Phi_{\mathcal{Y}}(\mathbf{t})| + 2|\Phi_{\mathcal{X}}(\mathbf{t})||\Phi_{\mathcal{Y}}(\mathbf{t})|(1 - \cos(\mathbf{a}_{\mathcal{X}}(\mathbf{t}) - \mathbf{a}_{\mathcal{Y}}(\mathbf{t}))) \\ &= \underbrace{(|\Phi_{\mathcal{X}}(\mathbf{t})| - |\Phi_{\mathcal{Y}}(\mathbf{t})|)^2}_{\text{amplitude difference}} + 2|\Phi_{\mathcal{X}}(\mathbf{t})||\Phi_{\mathcal{Y}}(\mathbf{t})|\underbrace{(1 - \cos(\mathbf{a}_{\mathcal{X}}(\mathbf{t}) - \mathbf{a}_{\mathcal{Y}}(\mathbf{t})))}_{\text{phase difference}}, \end{aligned} \quad (5)$$

where $\mathbf{a}_{\mathcal{X}}(\mathbf{t})$ and $\mathbf{a}_{\mathcal{Y}}(\mathbf{t})$ represent the angles (phases) of $\Phi_{\mathcal{X}}(\mathbf{t})$ and $\Phi_{\mathcal{Y}}(\mathbf{t})$, respectively. Therefore, we can clearly see that $\mathcal{C}_{\mathcal{T}}(\mathcal{X}, \mathcal{Y})$ basically measures the amplitude difference and the phase difference weighted by the amplitudes. We can further consider a convex combination of the two terms via $0 \leq \alpha \leq 1$, to yield

$$c_{\alpha}(\mathbf{t}) = \alpha ((|\Phi_{\mathcal{X}}(\mathbf{t})| - |\Phi_{\mathcal{Y}}(\mathbf{t})|)^2) + (1 - \alpha) (2|\Phi_{\mathcal{X}}(\mathbf{t})||\Phi_{\mathcal{Y}}(\mathbf{t})|(1 - \cos(\mathbf{a}_{\mathcal{X}}(\mathbf{t}) - \mathbf{a}_{\mathcal{Y}}(\mathbf{t})))). \quad (6)$$

Recall that for the elliptical distributions in Example 1, the phase represents the distribution centre while the amplitude represents the scale; $\mathcal{C}_{\mathcal{T}}(\mathcal{X}, \mathcal{Y})$ thus measures the both discrepancy of the centres and diversity of two distributions. We show in Figure 2-(a) that by swapping the phase and amplitude parts, the saliency information follows the phase part of the CF, which captures the centres of the distribution⁴. We further illustrate in Figure 2-(b) that this property still holds in real data distributions, even though they are much complicated and even non-unimodal. From Figure 2-(b)-(d), mainly training the phase (shown in Figure 2-(c)) results in generating images similar to an average of the real data, as a result of minimising the difference of the data centres. On the other hand, when mainly training the amplitude (shown in Figure 2-(b)), we can obtain diversified but inaccurate images (“wrong” numbers such as “1” for digit 7 and “6” for digit 5, uneven characters, disconnected artefacts, etc.). Therefore, by using different weights in $c_{\alpha}(\mathbf{t})$, we can flexibly capture the main content via minimising the phase difference, whilst enriching the diversity of generated images by increasing the amplitude loss. This provides a meaningful and feasible way of understanding the GAN loss in controlling the generation.

2.3 Sampling the Characteristic Function Loss

In practice, to calculate $\mathcal{C}_{\mathcal{T}}(\mathcal{X}, \mathcal{Y})$ efficiently, as mentioned in Section 2.1, $\Phi_{\mathcal{X}}(\mathbf{t})$ and $\Phi_{\mathcal{Y}}(\mathbf{t})$ can be evaluated by the ECFs of \mathcal{X} and \mathcal{Y} , which are weakly convergent to the corresponding population CFs. The remaining task is to sample from $F_{\mathcal{T}}(\mathbf{t})$. A direct approach is to use the neural net where the input is Gaussian noise and the output is the samples of $F_{\mathcal{T}}(\mathbf{t})$. However, Proposition 1 indicates that this can lead to ill-posed optima whereby $F_{\mathcal{T}}(\mathbf{t})$ converges to some point mass distributions and

⁴This phenomenon has been discovered in the Fourier representation of signals [37, 38]. We validate that this also holds in probabilistic distributions.

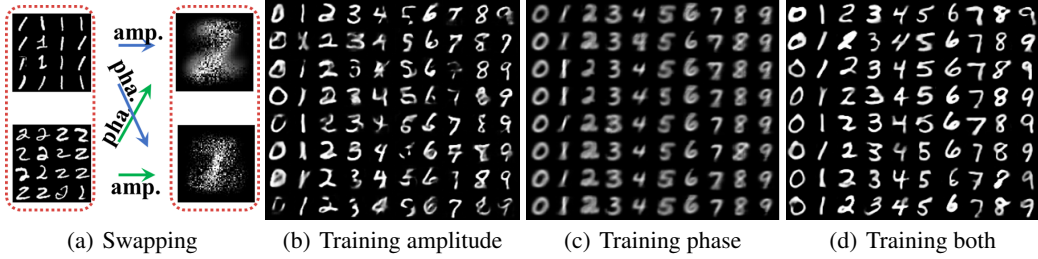


Figure 2: Two experiments on the MNIST dataset which show the physical meaning of the phase and amplitude of the CF. (a) A multivariate Gaussian fit to the images of digits 1 and 2, by naively assuming that each pixel is independent from other pixels. Then, the phase and amplitude information of the CFs between the two multivariate distributions were swapped, and then randomly sampled from the swapped distributions. (b)-(d) A generator was directly trained on the given images of each digit. To avoid the impact from the *critic*, we *DO NOT* employ the *critic* in this experiment but directly calculate the loss between images after the generator with different α . We performed training for amplitude for $\alpha = 0.999$ in (b), phase only for $\alpha = 0.001$ in (c) and equally training the amplitude and phase information for $\alpha = 0.5$ in (d).

this is no longer supported in \mathbb{R}^m as required in Lemma 1. In other words, for the degenerated $F_{\mathcal{T}}(\mathbf{t})$, we may have $\mathcal{C}_{\mathcal{T}}(\mathcal{X}, \mathcal{Y})$ but $\mathcal{X} \neq \mathcal{Y}$. In our experiment, we also found that directly optimising $F_{\mathcal{T}}(\mathbf{t})$ can cause instability.

Proposition 1. *The maximum of $\mathcal{C}_{\mathcal{T}}(\mathcal{X}, \mathcal{Y})$ is reached when $F_{\mathcal{T}}(\mathbf{t})$ attains a mass point at \mathbf{t}^* , where $\mathbf{t}^* = \arg \max_{\mathbf{t}} c(\mathbf{t})$. The minimum of $\mathcal{C}_{\mathcal{T}}(\mathcal{X}, \mathcal{Y})$ is reached when $F_{\mathcal{T}}(\mathbf{t})$ attains a mass point at $\mathbf{0}$.*

In the way of addressing this ill-posed optimisation on $F_{\mathcal{T}}(\mathbf{t})$, we can impose some constraints on $F_{\mathcal{T}}(\mathbf{t})$, for example, by assuming some parametric distributions. On the other hand, we may also be concerned that the constraints on $F_{\mathcal{T}}(\mathbf{t})$ can impede the ability of $\mathcal{C}_{\mathcal{T}}(\mathcal{X}, \mathcal{Y})$ as a metric to distinguish \mathcal{X} from \mathcal{Y} . Lemma 2 provides an efficient and feasible way of choosing $F_{\mathcal{T}}(\mathbf{t})$.

Lemma 2. *If \mathcal{X} and \mathcal{Y} are supported on a finite interval $[-1, 1]^m$, $\mathcal{C}_{\mathcal{T}}(\mathcal{X}, \mathcal{Y})$ in (4) is still a distance metric for distinguishing \mathcal{X} from \mathcal{Y} for any $F_{\mathcal{T}}(\mathbf{t})$ that samples \mathbf{t} within a small ball about $\mathbf{0}$.*

As shown in the next section, we employ $\mathcal{C}_{\mathcal{T}}(\mathcal{X}, \mathcal{Y})$ as the loss to compare two distributions from the *critic*. By employing bounded activation functions (tanh, sigmoid, etc.), the requirement of Lemma 2 is automatically satisfied, where the Lipschitz condition is also ensured given the local Lipschitz of a regular neural network [5]. Therefore, instead of searching within all the real distribution spaces, the choices of $F_{\mathcal{T}}(\mathbf{t})$ can be safely restricted to some zero-mean distributions, e.g., the Gaussian distribution. Furthermore, compared to the fixed Gaussian distribution, it is preferable, whilst avoiding the ill-posed optimum, that $F_{\mathcal{T}}(\mathbf{t})$ could be optimised to better accommodate the difference between two distributions.

In this paper, we choose $F_{\mathcal{T}}(\mathbf{t})$ as the cdf of a broad class of distributions called the *scale mixture of normals*, in the form of

$$p_{\mathcal{T}}(\mathbf{t}) = \int_{\Sigma} p_{\mathcal{N}}(\mathbf{t}|\mathbf{0}, \Sigma) p_{\Sigma}(\Sigma) d\Sigma, \quad (7)$$

where $p_{\mathcal{T}}(\mathbf{t})$ is the pdf of $F_{\mathcal{T}}(\mathbf{t})$, while $p_{\mathcal{N}}(\mathbf{t}|\mathbf{0}, \Sigma)$ denotes the zero-mean Gaussian distribution with the covariance given by Σ , and $p_{\Sigma}(\Sigma)$ denotes distributions of Σ . It needs to be pointed out that the *scale mixture of normals* constitutes a large portion of the elliptical distributions and includes many important distributions (e.g., the Gaussian, Cauchy, Student- t , hyperbolic distributions [39]) by choosing different $p_{\Sigma}(\Sigma)$. Therefore, instead of directly optimising $F_{\mathcal{T}}(\mathbf{t})$, which leads to ill-posed solutions, we alternatively optimise the neural net to output the samples of $p_{\Sigma}(\Sigma)$. By using the affine transformation (or the re-parametrisation trick), we are able to propagate back the gradients.

We should point out that the term $\int_{\mathbf{t}} c(\mathbf{t}) dF_{\mathcal{T}}(\mathbf{t})$ contained in our CF loss can also be interpreted as certain well behaved kernels in the MMD metric. This is due to the fact that the shift invariant and characteristic kernels in the MMD metric have to satisfy $k(\mathbf{x}, \mathbf{y}) = \int_{\mathbf{t}} e^{-j\mathbf{t}^T(\mathbf{x}-\mathbf{y})} dF_{\mathcal{T}}(\mathbf{t})$ for some compactly supported $F_{\mathcal{T}}(\mathbf{t})$ [40]. In contrast to the predefined and fixed kernels in the MMD-GANs, the proposed optimisation on the types of $F_{\mathcal{T}}(\mathbf{t})$ is thus able to learn this important hyperparameter, i.e., the type of kernels. On the other hand, the elliptical distributions in Example 1 potentially provide a set of well-defined characteristic kernels, by choosing $F_{\mathcal{T}}(\mathbf{t})$ as a normalised version of the CFs in (3). Then, the corresponding real-valued kernels are the density generators in [19].

3 Reciprocal Adversarial Learning

3.1 Characteristic Function Loss in RCF-GAN

Although the CF loss is a complete metric for measuring any forms of data distributions (e.g., Fig. 2-(b)-(d)), the CF loss in (4) works more efficiently and effectively in the embedded domain, with higher likelihood of learning fruitful representations of data. To this end, we first express our RCF-GAN in the IPM-GAN format as

$$d(\mathcal{P}_d, \mathcal{P}_g) = \sup_{\mathcal{T}, f \in \mathcal{F}} \mathcal{C}_{\mathcal{T}}(f(\overline{\mathcal{X}}), f(\overline{\mathcal{Y}})), \quad \overline{\mathcal{X}} \sim \mathcal{P}_d \text{ and } \overline{\mathcal{Y}} \sim \mathcal{P}_g, \quad (8)$$

where we make a distinction between the random variables ($\overline{\mathcal{X}}$ and $\overline{\mathcal{Y}}$) in the data domain and those (\mathcal{X} and \mathcal{Y}) in the embedded domain, i.e., $\mathcal{X} =^d f(\overline{\mathcal{X}})$ and $\mathcal{Y} =^d f(\overline{\mathcal{Y}})$. Lemma 3 below shows that this metric is well-defined for neural net training.

Lemma 3. *The metric $\mathcal{C}_{\mathcal{T}}(\mathcal{X}, \mathcal{Y})$ is bounded and differentiable almost everywhere.*

Because $\mathcal{C}_{\mathcal{T}}(\cdot, \cdot)$ is bounded by construction, it relaxes the requirements on the *critic* $f \in \mathcal{F}$. Otherwise, we may need to bound \mathcal{F} to ensure the existence of the supremum [10].

3.2 Matching in the Embedded Space

Having proved that $\mathcal{C}_{\mathcal{T}}(\mathcal{X}, \mathcal{Y}) = 0 \Leftrightarrow \mathcal{X} =^d \mathcal{Y}$, we also need to prove the equivalence between $\mathcal{C}_{\mathcal{T}}(f(\overline{\mathcal{X}}), f(\overline{\mathcal{Y}})) = 0$ and $\overline{\mathcal{X}} =^d \overline{\mathcal{Y}}$, to ensure that our RCF-GAN correctly learns the real distribution in the data domain. This result is provided in Lemma 4.

Lemma 4. *Denote the distribution mapping by $\overline{\mathcal{Y}} =^d g(\mathcal{Z})$. Given two functions $f(\cdot)$ and $g(\cdot)$ that map between the supports of $\overline{\mathcal{Y}}$ and \mathcal{Z} , if $\mathbb{E}_{\mathcal{Z}}[\|\mathbf{z} - f(g(\mathbf{z}))\|_2^2] = 0$, we also have the reciprocal property $\mathbb{E}_{\overline{\mathcal{Y}}}[\|\overline{\mathbf{y}} - g(f(\overline{\mathbf{y}}))\|_2^2] = 0$, and vice versa. More importantly, this yields the following equivalences: $\mathcal{C}_{\mathcal{T}}(f(\overline{\mathcal{X}}), f(\overline{\mathcal{Y}})) = 0 \Leftrightarrow \mathcal{C}_{\mathcal{T}}(\overline{\mathcal{X}}, \overline{\mathcal{Y}}) = 0 \Leftrightarrow \mathcal{C}_{\mathcal{T}}(f(\overline{\mathcal{Y}}), \mathcal{Z}) = 0$ and $\mathcal{C}_{\mathcal{T}}(f(\overline{\mathcal{X}}), \mathcal{Z}) = 0$.*

As a prerequisite of Lemma 4, the co-domains between $f(\cdot)$ and $g(\cdot)$ need to reside on the supports of $\overline{\mathcal{Y}}$ and \mathcal{Z} . Otherwise, the reciprocal may not hold. In our RCF-GAN, we propose an anchor design to our *critic*, by rewriting the *critic* loss (by minimising) as $-(\mathcal{C}_{\mathcal{T}}(f(\overline{\mathcal{Y}}), \mathcal{Z}) - \mathcal{C}_{\mathcal{T}}(f(\overline{\mathcal{X}}), \mathcal{Z}))$. Thus, \mathcal{Z} operates as the static anchor (or pivot) in the dynamic training process. Besides stabilising and improving the convergence in training, this further enables the *critic* to quickly map real data, $\overline{\mathcal{X}}$, to the support of \mathcal{Z} , whilst the generator tries to map the generated distribution, $\overline{\mathcal{Y}}$, to the real data, $\overline{\mathcal{X}}$. The adversarial part to maximise $\mathcal{C}_{\mathcal{T}}(f(\overline{\mathcal{Y}}), \mathcal{Z})$ aims to improve the generation quality against the generator loss, i.e., $\mathcal{C}_{\mathcal{T}}(f(\overline{\mathcal{X}}), f(\overline{\mathcal{Y}}))$. Fig. 1 illustrates the triangle relationship in our anchor design.

Furthermore, Lemma 4 indicates that instead of being regarded as components of some IPMs (e.g., the W-GAN) to be optimised with strict restrictions, the *critic* can be basically regarded as a feature mapping because in the embedded domain the CF loss is a valid distance metric of distributions. The *critic* can then be relaxed to satisfy the reciprocal property. Therefore, we incorporate the auto-encoder in only two modules by interchangeably treating the *critic* as the encoder and the generator as the decoder. More importantly, Lemma 4 ensures that matching in the embedded space is sufficient due to $\mathbb{E}_{\mathcal{Z}}[\|\mathbf{z} - f(g(\mathbf{z}))\|_2^2] = 0 \rightarrow \mathbb{E}_{\overline{\mathcal{Y}}}[\|\overline{\mathbf{y}} - g(f(\overline{\mathbf{y}}))\|_2^2] = 0$. This is beneficial in various applications such as the image generation (and reconstruction), where in the data domain, the MSE loss typically leads to smooth artefacts.

3.3 Putting Everything Together

In practice, in Lemma 4, we regard $f(\cdot)$ as the *critic* and $g(\cdot)$ as the generator. The t -net is denoted by $h(\cdot)$ and the covariance matrix of its output is assumed to be diagonal (we thus represent it as σ), which is reasonable as in the embedded domain the multiple dimensions tend to be uncorrelated [41]. We also need to clarify that because the t -net is optional and in our RCF-GAN, fixed Gaussian can be directly sampled for \mathbf{t} , we separate the t -net from $f(\cdot)$. However, if the t -net is employed, since they (the t -net and *critic*) have the same goal of distinguishing the generated distribution from the real data distribution, they are optimised simultaneously and share the same *critic* loss, i.e., $-(\mathcal{C}_{\mathcal{T}}(f(\overline{\mathcal{Y}}), \mathcal{Z}) - \mathcal{C}_{\mathcal{T}}(f(\overline{\mathcal{X}}), \mathcal{Z}))$. Moreover, the *critic* additionally minimises an MSE loss to ensure the reciprocal property. On the other hand, the generator is trained by minimising (8) as usual. The pseudo-code for the proposed RCF-GAN is provided in Algorithm 1.

It also needs to be pointed out that here we choose \mathcal{Z} as the Gaussian distribution for a fair comparison to other GANs; other complex distributions can be seamlessly adopted in our framework

according to different tasks, for example, finite mixture models for un-supervised and semi-supervised classifications, and learnt distributions for sequential data processing.

Remark 1. Besides the case of computation, the structure of the proposed RCF-GAN benefits from its interpretation as both a GAN and an auto-encoder, as a way of unifying them. As an auto-encoder, the RCF-GAN enables us to compare reconstructions solely on a meaningful embedded manifold, instead of in the data domain. When regarded as a GAN, the auto-encoder part theoretically and practically indicates the convergence; it also stabilises the training by pushing the embedded distributions to the static anchor \mathcal{Z} .

Algorithm 1: RCF-GAN. In all the experiments in this paper, the generator and the *critic* are trained once at each iteration. The optional *t*-net with parameter θ_t is designated by $h_{\theta_t}(\cdot)$.

input: Real data distribution \mathcal{P}_d ; Gaussian noise \mathcal{P}_N ; batch sizes b_d, b_g, b_t and b_σ for the data, the generator input noise, \mathcal{T} and *t*-net input noise, respectively; learning rate l_r ; reciprocal regularisation in the embedded domain λ

output: Net parameters θ_c and θ_g for the *critic* and generator, respectively

while θ_c and θ_g not converge **do**

 /* train the *critic* */

 Sample from distributions: $\{\bar{\mathbf{x}}_i\}_{i=1}^{b_d} \sim \mathcal{P}_d$; $\{\mathbf{z}_i\}_{i=1}^{b_g} \sim \mathcal{P}_N$; $\{\mathbf{t}_i\}_{i=1}^{b_t} \sim \mathcal{P}_N$; $\{\sigma_i\}_{i=1}^{b_\sigma} \sim \mathcal{P}_N$

 Affine transform: $\{\mathbf{t}_i\}_{i=1}^{b_t} \leftarrow (\{\mathbf{t}_i\}_{i=1}^{b_t}, h_{\theta_t}(\{\sigma_i\}_{i=1}^{b_\sigma}))$ // optional

 Calculate adversarial loss: // empirical version of $-(\mathcal{C}_{\mathcal{T}}(f(\bar{\mathcal{Y}}), \mathcal{Z}) - \mathcal{C}_{\mathcal{T}}(f(\bar{\mathcal{X}}), \mathcal{Z}))$

$$\mathcal{L} = -(\mathcal{C}_{\{\mathbf{t}_i\}_{i=1}^{b_t}}(f_{\theta_c}(g_{\theta_g}(\{\mathbf{z}_i\}_{i=1}^{b_g})), \{\mathbf{z}_i\}_{i=1}^{b_g}) - \mathcal{C}_{\{\mathbf{t}_i\}_{i=1}^{b_t}}(f_{\theta_c}(\{\bar{\mathbf{x}}_i\}_{i=1}^{b_d}), \{\mathbf{z}_i\}_{i=1}^{b_g}))$$

 Update: $\theta_t \leftarrow \theta_t + l_r \cdot \text{Adam}(\theta_t, \nabla_{\theta_t}[\mathcal{L}])$

$$\theta_c \leftarrow \theta_c + l_r \cdot \text{Adam}(\theta_c, \nabla_{\theta_c}[\mathcal{L} + \lambda \sum_{i=1}^{b_g} \|\mathbf{z}_i - f_{\theta_c}(g_{\theta_g}(\mathbf{z}_i))\|_2^2])$$

 /* train the generator */

 Sample from distributions: $\{\bar{\mathbf{x}}_i\}_{i=1}^{b_d} \sim \mathcal{P}_d$; $\{\mathbf{z}_i\}_{i=1}^{b_g} \sim \mathcal{P}_N$; $\{\mathbf{t}_i\}_{i=1}^{b_t} \sim \mathcal{P}_N$; $\{\sigma_i\}_{i=1}^{b_\sigma} \sim \mathcal{P}_N$

 Affine transform: $\{\mathbf{t}_i\}_{i=1}^{b_t} \leftarrow (\{\mathbf{t}_i\}_{i=1}^{b_t}, h_{\theta_t}(\{\sigma_i\}_{i=1}^{b_\sigma}))$ // optional

 Calculate adversarial loss: // empirical version of $\mathcal{C}_{\mathcal{T}}(f(\bar{\mathcal{Y}}), f(\bar{\mathcal{X}}))$

$$\mathcal{L} = \mathcal{C}_{\{\mathbf{t}_i\}_{i=1}^{b_t}}(f_{\theta_c}(g_{\theta_g}(\{\mathbf{z}_i\}_{i=1}^{b_g})), f_{\theta_c}(\{\bar{\mathbf{x}}_i\}_{i=1}^{b_d}))$$

 Update: $\theta_g \leftarrow \theta_g + l_r \cdot \text{Adam}(\theta_g, \nabla_{\theta_g}[\mathcal{L}])$

4 Experimental Results

In this section, our RCF-GAN is evaluated in terms of both image generation, reconstruction and interpolation, with our code available at https://github.com/ShengxiLi/rcf_gan. We also show in the supplementary material advanced results including phase and amplitude analysis, ablation study and superior performances under the ResNet structure.

Datasets: Three widely applied benchmark datasets were employed in the evaluation: CelebA (faces of celebrities) [44], CIFAR-10 [45] and LSUN Bedroom (LSUN_B) [46]. The images of the CelebA and LSUN_B were cropped to the size 64×64 , whilst the image size of the CIFAR10 was 32×32 . When evaluating the reconstruction, the test sets of the CIFAR10 and LSUN_B were employed, of which the samples were not used in the training.

Baselines: As our work is mainly related to the IPM-GANs, we compared our RCF-GAN with the W-GAN [5], W-GAN with gradient penalty (W-GAN-GP) [8] and MMD-GAN [13, 14]. As an advancement of the MMD-GAN, the most recent work, OCF-GAN [27], together with its gradient penalty version (OCF-GAN-GP) was also compared. We need to point out that all the results reported in [27] were evaluated for the image size of 32×32 . We thus ran the experiments for the CelebA and LSUN_B for image sizes 64×64 by using its provided code. For image reconstruction, we compared our RCF-GAN with the recent adversarial generator-encoder (AGE) work [20], which empirically performs better than the adversarially learned inference (ALI) [26].

Metrics: The Fréchet inception distance (FID) [43] was employed as a performance metric, which is basically the Wasserstein distance between two Gaussian distributions, together with the kernel inception distance (KID) that arises from the MMD metric [14]. In evaluating the FID and KID scores, we randomly generated 25,000 samples for both generation and true images, and obtained these metrics in terms of mean and standard deviation by 10 times repeated random selections.

Table 1: The FID and KID scores obtained from the DCGAN [42] structure. The results of the DCGAN and W-GAN-GP are from [43] and [14]. The corresponding publicly available codes were run to obtain the results of the W-GAN [5], MMD-GAN [13], OCF-GAN and OCF-GAN-GP [27]. The results of the AGE were tested from its pre-trained models [20].

Methods	FID			KID		
	CIFAR-10	Celeba	LSUN_B	CIFAR-10	Celeba	LSUN_B
DCGAN	37.7 [43]	21.4 [43]	70.4 [43]	---	---	---
W-GAN	42.64±0.26	31.85±0.28	57.05±0.37	0.025±0.001	0.023±0.001	0.048±0.002
W-GAN-GP	37.52±0.19[14]	---	41.39±0.25[14]	0.026±0.001[14]	---	0.039±0.002[14]
MMD-GAN	42.8±0.27	32.5±0.16	56.52±0.34	0.025±0.001	0.024±0.001	0.047±0.002
OCF-GAN	40.99±0.15	32.66±0.16	61.48±0.23	0.024±0.001	0.024±0.001	0.052±0.002
OCF-GAN-GP	33.68±0.21	16.09±0.25	65.18±0.317	0.021±0.001	0.011±0.001	0.060±0.002
AGE	32.54±0.24	23.19±0.14	---	0.020±0.001	0.017±0.001	---
RCF-GAN _(t_norm)	31.55±0.20	19.34±0.22	38.16±0.286	0.019±0.001	0.012±0.001	0.032±0.001
RCF-GAN _(t_net)	31.21±0.21	15.86±0.08	40.15±0.40	0.018±0.001	0.011±0.001	0.034±0.001
AGE(R)	47.37±0.32	30.77±0.19	---	0.022±0.001	0.024±0.001	---
RCF-GAN _(t_net) (R)	28.70±0.16	14.82±0.12	44.16±0.42	0.014±0.001	0.009±0.000	0.036±0.001

Note: t_norm corresponds to use the fixed Gaussian samples and t_net to the t -net. (R) denotes for the reconstruction.

Net structure and technical details: For a fair comparison, all the reported results were compared under the batch sizes of 64 (i.e., $b_d = b_g = b_t = b_\sigma = 64$). Moreover, all variances of Gaussian noise were set to 1, except for the input noise of the generator that was 0.3, because the reciprocal loss had to be minimised given the fact that the output of the *critic* is restricted to $[-1, 1]$. Furthermore, we do not require the Lipschitz constraint, which allows for a relatively larger learning rate ($l_r = 0.0002$ for both nets). Moreover, for the CIFAR10 and LSUN_B datasets, the dimension of the embedded domain was set to 128 and for the CelebA dataset the dimension was 64. The optional t -net, if used, was a small three layer fully connected net, with the dimension of each layer being the same as the embedded dimension. Our default RCF-GAN used t -net and layer normalisation, and was trained with the vanilla CF loss (i.e., $\alpha = 0.5$ in (6)).

Image generation: The images generated from random Gaussian noise are shown in Fig. 3. Observe that by using the proposed CF loss in the RCF-GAN, the generated images are clear and close to the real images; the FID and KID scores are further provided in Table 1. This table shows that the proposed RCF-GAN consistently achieved the best performances across the three datasets. The OCF-GAN-GP achieved comparable generation performance on the CelebA dataset, but had relatively inferior performances compared to our RCF-GAN on the CIFAR-10 and LSUN_B datasets. Thus, although the most recent independent work, OCF-GAN, also adopts the characteristic function in designing the loss, it still operates under the MMD-GAN framework, without the interpretation of the physical meaning of the characteristic function and the consideration of the t -net proposed in this paper. More importantly, the reciprocal structure introduced in this paper, together with the proposed CF loss, stably and significantly improves the image generation performance.

By inspecting the achieved best performances of RCF-GAN, the use of the t -net in outputting optimal $F_{\mathcal{T}}(t)$ proved beneficial. Moreover, solely training $g(\mathbf{z})$ via the CF typically performs inferior, which in our experiments on CelebA, obtained a 165 FID score (i.e., rough faces). This also verifies the benefit of latent space comparison via our critic. We also need to point out that in the default setting, our *critic* and generator were evaluated under almost the same number of model parameters as W-GANs, whereas MMD-GANs need an extra decoder net. The only extra cost in our t -net is negligible because it is a 3-layer fully connected net with the dimension of each layer less than 128.

More importantly, compared to a fluctuated generator loss that is caused by the adversarial module in GANs, we take the advantages of the auto-encoder structure in utilising the reciprocal loss (i.e., $\mathbb{E}_{\mathcal{Z}}[\|\mathbf{z} - f(g(\mathbf{z}))\|_2^2]$ indicates the reciprocal loss in the embedded space), together with the distance between the embedded real distribution $f(\mathcal{X})$ and the Gaussian distribution \mathcal{Z} (i.e., $\mathcal{C}_{\mathcal{T}}(f(\mathcal{X}), \mathcal{Z})$) to better indicate the convergence, as shown in Figure 3. Intuitively, the reciprocal loss measures the convergence on reconstructions, whereas the real image embedding distance $\mathcal{C}_{\mathcal{T}}(f(\mathcal{X}), \mathcal{Z})$ indicates the performance on generating images.

Image reconstruction: Benefiting from the reciprocal requirement introduced in Lemma 4, the proposed RCF-GAN can also reconstruct images and learn a semantic meaningful space. Images reconstructed and interpolated by RCF-GAN, AGE and MMD-GAN are shown in Fig. 4. As seen from this figure, because the RCF-GAN only matches the distributions in the embedded domain, the reconstructed images are thus clear and semantically meaningful, resulting in a superior interpolation

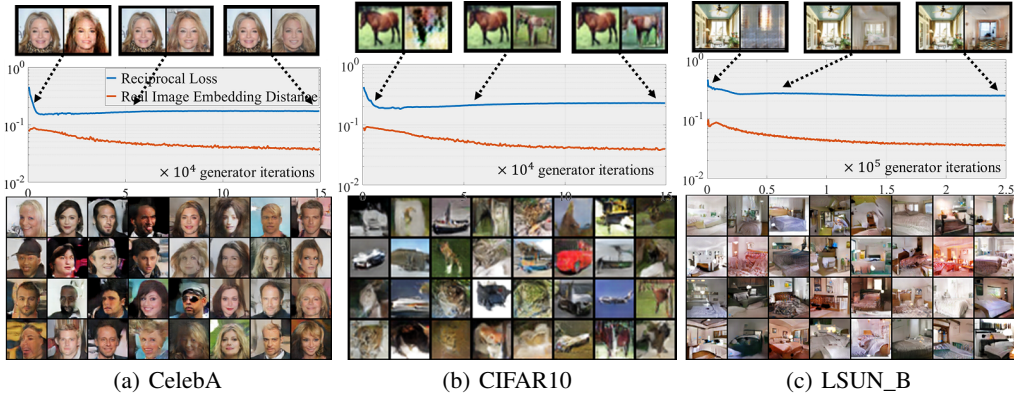


Figure 3: The convergence curves and images generated by the proposed RCF-GAN from Gaussian noise, under the DCGAN [42] structure. Note that the curves were plotted by an average over a moving window, with 500 iterations.

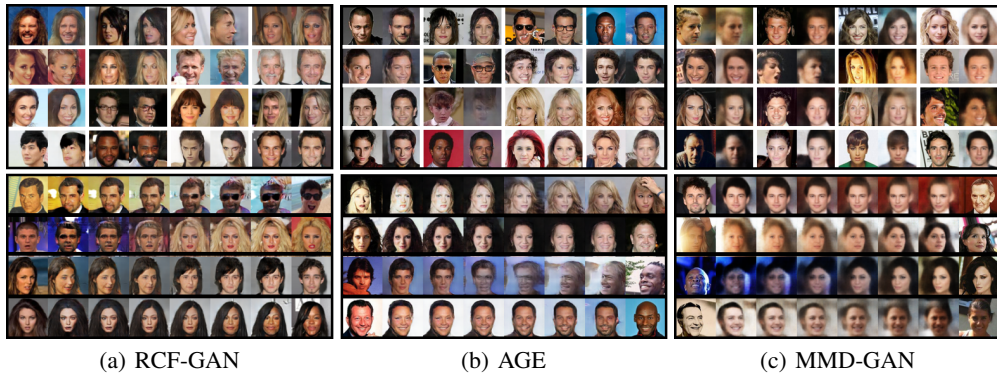


Figure 4: Image reconstruction (upper panel) and interpolation (lower panel) by the proposed RCF-GAN, AGE [20] and MMD-GAN [13] in the CelebA dataset, under the DCGAN [42] structure. The upper panel shows the reconstructed images (in even columns) corresponding to the original images (in odd columns). The lower panel displays the linear interpolation in the embedded domain.

and reconstruction. This is beneficial because besides randomly generating real images, RCF-GAN is able to bi-directionally reconstruct and interpolate real images. In contrast, although MMD-GANs employ a third module to implement an auto-encoder, the decoded images are severely blurred.

Moreover, the proposed RCF-GAN subjectively achieved better reconstruction and interpolation than the AGE, by generating less blurred and more accurate images (for example, correct skin and hair colours). This is quantified in Table 1, which shows that the images reconstructed by our RCF-GAN are superior to those from the AGE. More importantly, by comparing with the FID and KID scores in Table 1, the images from the proposed RCF-GAN are consistently superior, whilst the quality of the reconstructed images in the AGE is significantly inferior to its random generated images. This also indicates the effectiveness of the unified structure of our RCF-GAN.

5 Conclusion

We have introduced an efficient generative adversarial net (GAN) structure that seamlessly combines the IPM-GANs and auto-encoders. In this way, the reciprocal in the proposed RCF-GAN ensures the equivalence between the embedded and data domains, whereas in the embedded domain the comparison of two distributions is strongly supported by the proposed powerful characteristic function (CF) loss, together with the physically meaningful phase and amplitude information, and an efficient sampling strategy. The reciprocal, accompanied with the proposed anchor design, has been shown to also stabilise the convergence of the adversarial learning in the proposed RCF-GAN, and at the same time to benefit from meaningful comparisons in the embedded domain. Consequently, the experimental results have demonstrated the superior performances of our RCF-GAN in both generating images and reconstructing images.

6 Broader Impact

A combination of the auto-encoder and GANs has been extensively studied, and has been shown to achieve a broader data generation and reconstruction. The RCF-GAN proposed in this paper provides a neat and new structure in the combination. The studies of GANs and those design on probabilistic auto-encoders basically start from different perspectives because the former serves for the generation, or it “decodes” from random noise, whilst the latter, as its name implies, focuses on encoding to summarise information. Although there are extensive attempts on combining those two structures, they typically embed one into the other as components such as by using an auto-encoder as a discriminator in GANs or using an adversarial idea in an auto-encoder. This paper provides a way of equally treating the two structures; the proposed structure, which contains only two modules, can be regarded both as an “encoder-decoder” and “discriminator-generator”. The proposed combination benefits both, that is, it equips an auto-encoder the ability to meaningfully encode via matching in the embedded domain, whilst ensuring the convergence of the adversarial as a GAN.

Moreover, instead of being a component to measure the distance as in the W-GAN, regarding the *critic* as an independent feature mapping module with a sufficient distance metric is beneficial to allow learning in the embedded domain for any types of feature extraction models, such as the deep canonical correlation analysis net and graph auto encoder. A large amount of unsupervised learning models, then, can be connected and improved with the adversarial learning.

Another potential benefit of our work is to bring the general concept of the characteristic function (CF) into practice, by providing efficient sampling methods. The CF has been previously studied as a powerful tool in theoretical probabilistic analysis, while its practical applications have been limited due to complex functional forms. We should also highlight the physical meaning of the CF components introduced in this paper. It is a well known experimental phenomenon that the phase of discrete Fourier transform of images captures the saliency information, which motivates a large volume of works in saliency detection. This paper gives a probabilistic explanation to this, paving the way for future work to embark upon this intrinsic relationship.

Acknowledgments and Disclosure of Funding

Shengxi Li wishes to thank Imperial Lee Family Scholarship for the support of his research.

References

- [1] Ian Goodfellow, Jean Pouget-Abadie, Mehdi Mirza, Bing Xu, David Warde-Farley, Sherjil Ozair, Aaron Courville, and Yoshua Bengio. Generative adversarial nets. In *Advances in Neural Information Processing Systems*, pages 2672–2680, 2014.
- [2] Lars Mescheder, Andreas Geiger, and Sebastian Nowozin. Which training methods for GANs do actually converge? *arXiv preprint arXiv:1801.04406*, 2018.
- [3] Martín Arjovsky and Léon Bottou. Towards principled methods for training generative adversarial networks. *ArXiv*, abs/1701.04862, 2017.
- [4] Alfred Müller. Integral probability metrics and their generating classes of functions. *Advances in Applied Probability*, 29(2):429–443, 1997.
- [5] Martin Arjovsky, Soumith Chintala, and Léon Bottou. Wasserstein GAN. *arXiv preprint arXiv:1701.07875*, 2017.
- [6] Sanjeev Arora, Rong Ge, Yingyu Liang, Tengyu Ma, and Yi Zhang. Generalization and equilibrium in generative adversarial nets (GANs). In *Proceedings of the 34th International Conference on Machine Learning*, pages 224–232. JMLR. org, 2017.
- [7] Sanjeev Arora and Yi Zhang. Do GANs actually learn the distribution? An empirical study. *arXiv preprint arXiv:1706.08224*, 2017.
- [8] Ishaan Gulrajani, Faruk Ahmed, Martin Arjovsky, Vincent Dumoulin, and Aaron C Courville. Improved training of Wasserstein GANs. In *Advances in Neural Information Processing Systems*, pages 5767–5777, 2017.

- [9] Takeru Miyato, Toshiki Kataoka, Masanori Koyama, and Yuichi Yoshida. Spectral normalization for generative adversarial networks. *arXiv preprint arXiv:1802.05957*, 2018.
- [10] Youssef Mroueh and Tom Sercu. Fisher GAN. In *Advances in Neural Information Processing Systems*, pages 2513–2523, 2017.
- [11] Youssef Mroueh, Tom Sercu, and Vaibhava Goel. McGAN: Mean and covariance feature matching gan. *arXiv preprint arXiv:1702.08398*, 2017.
- [12] Sung Woo Park and Junseok Kwon. Sphere generative adversarial network based on geometric moment matching. In *Proceedings of the IEEE Conference on Computer Vision and Pattern Recognition*, pages 4292–4301, 2019.
- [13] Chun-Liang Li, Wei-Cheng Chang, Yu Cheng, Yiming Yang, and Barnabás Póczos. MMD gan: Towards deeper understanding of moment matching network. In *Advances in Neural Information Processing Systems*, pages 2203–2213, 2017.
- [14] Mikołaj Bińkowski, Dougal J Sutherland, Michael Arbel, and Arthur Gretton. Demystifying MMD GANs. *arXiv preprint arXiv:1801.01401*, 2018.
- [15] Farzan Farnia and David Tse. A convex duality framework for GANs. In *Advances in Neural Information Processing Systems*, pages 5248–5258, 2018.
- [16] Shuang Liu, Olivier Bousquet, and Kamalika Chaudhuri. Approximation and convergence properties of generative adversarial learning. In *Advances in Neural Information Processing Systems*, pages 5545–5553, 2017.
- [17] Shakir Mohamed and Balaji Lakshminarayanan. Learning in implicit generative models. *arXiv preprint arXiv:1610.03483*, 2016.
- [18] Youssef Mroueh, Chun-Liang Li, Tom Sercu, Anant Raj, and Yu Cheng. Sobolev GAN. *arXiv preprint arXiv:1711.04894*, 2017.
- [19] Shengxi Li, Zeyang Yu, Min Xiang, and Danilo Mandic. Solving general elliptical mixture models through an approximate Wasserstein manifold. *arXiv preprint arXiv:1906.03700*, 2019.
- [20] Dmitry Ulyanov, Andrea Vedaldi, and Victor Lempitsky. It takes (only) two: Adversarial generator-encoder networks. In *Thirty-Second AAAI Conference on Artificial Intelligence*, 2018.
- [21] Alireza Makhzani, Jonathon Shlens, Navdeep Jaitly, Ian Goodfellow, and Brendan Frey. Adversarial autoencoders. *arXiv preprint arXiv:1511.05644*, 2015.
- [22] Anders Boesen Lindbo Larsen, Søren Kaae Sønderby, Hugo Larochelle, and Ole Winther. Autoencoding beyond pixels using a learned similarity metric. *arXiv preprint arXiv:1512.09300*, 2015.
- [23] Jeff Donahue, Philipp Krähenbühl, and Trevor Darrell. Adversarial feature learning. *arXiv preprint arXiv:1605.09782*, 2016.
- [24] Andrew Brock, Theodore Lim, James M Ritchie, and Nick Weston. Neural photo editing with introspective adversarial networks. *arXiv preprint arXiv:1609.07093*, 2016.
- [25] Tong Che, Yanran Li, Athul Paul Jacob, Yoshua Bengio, and Wenjie Li. Mode regularized generative adversarial networks. *arXiv preprint arXiv:1612.02136*, 2016.
- [26] Vincent Dumoulin, Ishmael Belghazi, Ben Poole, Olivier Mastropietro, Alex Lamb, Martin Arjovsky, and Aaron Courville. Adversarially learned inference. *arXiv preprint arXiv:1606.00704*, 2016.
- [27] Abdul Fatir Ansari, Jonathan Scarlett, and Harold Soh. A characteristic function approach to deep implicit generative modeling. In *IEEE Conference on Computer Vision and Pattern Recognition*, 2020.
- [28] David Williams. *Probability with martingales*. Cambridge University Press, 1991.
- [29] Andrey Feuerverger, Roman A Mureika, et al. The empirical characteristic function and its applications. *The Annals of Statistics*, 5(1):88–97, 1977.
- [30] Eugene Lukacs. A survey of the theory of characteristic functions. *Advances in Applied Probability*, 4(1): 1–37, 1972.
- [31] TW Epps and Kenneth J Singleton. An omnibus test for the two-sample problem using the empirical characteristic function. *Journal of Statistical Computation and Simulation*, 26(3-4):177–203, 1986.

- [32] Kacper P Chwialkowski, Aaditya Ramdas, Dino Sejdinovic, and Arthur Gretton. Fast two-sample testing with analytic representations of probability measures. In *Advances in Neural Information Processing Systems*, pages 1981–1989, 2015.
- [33] Kai Wang Fang. *Symmetric multivariate and related distributions*. CRC Press, 2018.
- [34] Sergei Germanovich Bobkov. Proximity of probability distributions in terms of Fourier–Stieltjes transforms. *Russian Mathematical Surveys*, 71(6):1021, 2016.
- [35] Scott C Douglas and Danilo P Mandic. The least-mean-magnitude-phase algorithm with applications to communications systems. In *2011 IEEE International Conference on Acoustics, Speech and Signal Processing (ICASSP)*, pages 4152–4155. IEEE, 2011.
- [36] Zeyang Yu, Shengxi Li, and Danilo Mandic. Widely linear complex-valued autoencoder: Dealing with noncircularity in generative-discriminative models. In *International Conference on Artificial Neural Networks*, pages 339–350. Springer, 2019.
- [37] Alan V Oppenheim and Jae S Lim. The importance of phase in signals. *Proceedings of the IEEE*, 69(5): 529–541, 1981.
- [38] Danilo P Mandic and Vanessa Su Lee Goh. *Complex valued nonlinear adaptive filters: Noncircularity, widely linear and neural models*, volume 59. John Wiley & Sons, 2009.
- [39] David F Andrews and Colin L Mallows. Scale mixtures of normal distributions. *Journal of the Royal Statistical Society: Series B (Methodological)*, 36(1):99–102, 1974.
- [40] Bharath K Sriperumbudur, Arthur Gretton, Kenji Fukumizu, Bernhard Schölkopf, and Gert RG Lanckriet. Hilbert space embeddings and metrics on probability measures. *Journal of Machine Learning Research*, 11 (Apr):1517–1561, 2010.
- [41] Diederik P Kingma and Max Welling. Auto-encoding variational bayes. *arXiv preprint arXiv:1312.6114*, 2013.
- [42] Alec Radford, Luke Metz, and Soumith Chintala. Unsupervised representation learning with deep convolutional generative adversarial networks. *arXiv preprint arXiv:1511.06434*, 2015.
- [43] Martin Heusel, Hubert Ramsauer, Thomas Unterthiner, Bernhard Nessler, and Sepp Hochreiter. GANs trained by a two time-scale update rule converge to a local Nash equilibrium. In *Advances in Neural Information Processing Systems*, pages 6626–6637, 2017.
- [44] Ziwei Liu, Ping Luo, Xiaogang Wang, and Xiaoou Tang. Deep learning face attributes in the wild. In *Proceedings of the IEEE International Conference on Computer Vision*, pages 3730–3738, 2015.
- [45] Alex Krizhevsky, Geoffrey Hinton, et al. Learning multiple layers of features from tiny images. 2009.
- [46] Fisher Yu, Ari Seff, Yinda Zhang, Shuran Song, Thomas Funkhouser, and Jianxiong Xiao. Lsun: Construction of a large-scale image dataset using deep learning with humans in the loop. *arXiv preprint arXiv:1506.03365*, 2015.
- [47] Carl-Gustav Esseen et al. Fourier analysis of distribution functions: A mathematical study of the Laplace-Gaussian law. *Acta Mathematica*, 77:1–125, 1945.
- [48] K. Kreutz-Delgado. The complex gradient operator and the CR-calculus. *arXiv preprint arXiv:0906.4835*, 2009.
- [49] Marc G Bellemare, Ivo Danihelka, Will Dabney, Shakir Mohamed, Balaji Lakshminarayanan, Stephan Hoyer, and Rémi Munos. The Cramer distance as a solution to biased Wasserstein gradients. *arXiv preprint arXiv:1705.10743*, 2017.
- [50] David Berthelot, Thomas Schumm, and Luke Metz. Began: Boundary equilibrium generative adversarial networks. *arXiv preprint arXiv:1703.10717*, 2017.
- [51] Ishan Deshpande, Ziyu Zhang, and Alexander G Schwing. Generative modeling using the sliced Wasserstein distance. In *Proceedings of the IEEE Conference on Computer Vision and Pattern Recognition*, pages 3483–3491, 2018.

Table 2: Ablation study on the CelebA dataset. The proposed RCF-GAN was evaluated and compared to the one without (w/o) reciprocal requirement ($\lambda = 0$) and without anchor design.

FID			
	w/o reciprocal	w/o anchor	RCF-GAN
G.	59.39±0.37	17.80±0.20	15.86±0.08
R.	>100	>100	14.82±0.12
KID			
	w/o reciprocal	w/o anchor	RCF-GAN
G.	0.046±0.001	0.010±0.000	0.011±0.001
R.	>0.060	>0.060	0.009±0.000

Note: G. is for image random generation and R. for image reconstruction.

7 Appendix

7.1 In-depth Analysis

7.1.1 Phase and Amplitude in the CF Loss

We report the effects of α on training the overall RCF-GAN in Fig. 5. From this figure, we can find that the proposed RCF-GAN is robust to the choice of α , as when α ranges from 0.1 to 0.9, the RCF-GAN still achieved relatively superior generations. More importantly, we have not witnessed any mode collapse generations in all experiments. Although $\alpha = 0.5$ was a default and mainly used in our experiments, varying α could even achieve better performances. For example, for the dataset without complex and diversified scenarios (e.g., CelebA), imposing amplitude by $\alpha = 0.75$ increased the FID (KID) from 15.86 (0.011) to 13.84 (0.009). As the amplitude relates to the diversity measurement in the CF loss, the increment may come from enhancing the richness of generated faces. On the other hand, for some complicated scenarios (e.g., CIFAR-10), keeping the mean of data generation (that is, focusing on the phase) could be more beneficial (e.g., $\alpha = 0.1$).

Fig. 5 further shows an illustrative example on some over-weighted examples from CelebA. When over-weighting the phase ($\alpha = 0.1$), the generated images tend to be whitened and blurred, with their interpolation less smooth. This indicates that RCF-GAN tended to learn the average (mean) information of the data. On the contrary, when the amplitude was over-weighted ($\alpha = 0.9$), the generated images were over-saturated and with noisy artefacts, meaning that the RCF-GAN was likely to learn diversified content, even though some learnt faces were inaccurate. Therefore, the physical meaning of the proposed CF loss can provide a feasible way of understanding and evaluating generation details where the KID and FID metrics cannot reflect.

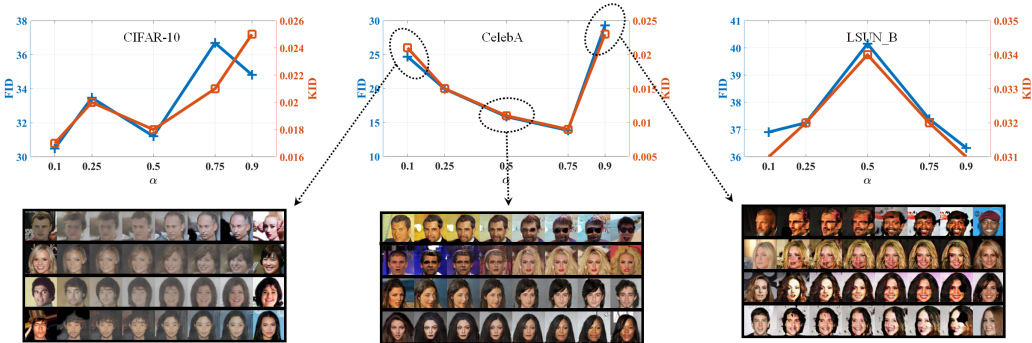


Figure 5: FID and KID scores for different α , under the DCGAN [42] structure. Observe the embedded space (by interpolated images) of the proposed RCF-GAN, which was learnt with different α on CelebA dataset.

7.1.2 Ablation Study

The roles of the two key distinguishing elements of the proposed RCF-GAN are now evaluated via an ablation study on the CelebA dataset. There are the term λ that controls the reciprocal together with the anchor design. The results in Table 2 showed that without the reciprocal loss (by setting $\lambda = 0$) the overall generation was

Table 3: The FID and KID scores under the ResNet structure in terms of 64×64 and 128×128 image sizes. The result of Sphere GAN was obtained from the original article [12]. We ran the available code of the OCF-GAN-GP [27] with its implemented ResNet structure because it failed to converge in our structure given in Fig. 6.

	FID		KID	
	Celeba	LSUN_B	Celeba	LSUN_B
64 × 64				
Sphere GAN	—	16.9 [12]	—	—
RCF-GAN	9.02±0.22	8.76±0.07	0.006±0.001	0.005±0.001
RCF-GAN (R.)	8.06±0.08	7.89±0.05	0.003±0.000	0.002±0.000
128 × 128				
OCF-GAN-GP	20.78±0.15	21.82±0.20	0.015±0.001	0.014±0.001
RCF-GAN	10.71±0.11	10.32±0.13	0.006±0.000	0.005±0.001
RCF-GAN (R.)	13.01±0.15	8.64±0.10	0.006±0.000	0.003±0.000

Note: R. is for image reconstruction.

largely degraded and the reconstruction even completely failed. This, on the one hand, highlights the necessity of the reciprocal loss in our work; on the other hand, it also validates the correctness of the theoretical guarantee in Lemma 4, which is an important requirement that also motivates the auto-encoder structure in our RCF-GAN. Moreover, Table 2 also validates the effectiveness of the proposed anchor design. Without the anchor design, the generation still works, however, because the minimisation of $\mathcal{C}_{\mathcal{T}}(f(\mathcal{X}), \mathcal{Z})$ by the anchor does no longer exist, the mapping of real images $f(\mathcal{X})$ might not completely fall into the support of \mathcal{Z} , thus leading to poor reconstructions. Therefore, in order to successfully generate and reconstruct images, the reciprocal and anchor architecture are necessary in the proposed RCF-GAN.

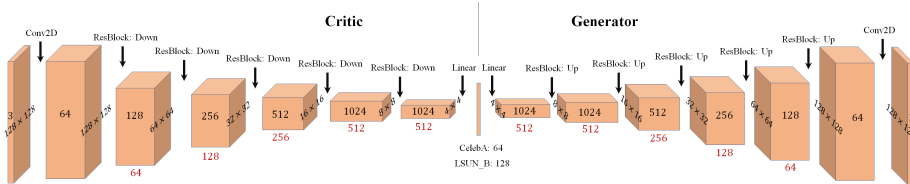


Figure 6: The ResNet 128×128 structure adopted in this work. Note that the numbers in red colour represent the channel setting of ResNet 64×64 .

7.2 Advancements under ResNet Structure

The scalability of the proposed RCF-GAN was further evaluated over complex net structures and higher image sizes. Specifically, we trained RCF-GAN under the ResNet structure, in terms of image sizes of 64×64 and 128×128 . The ResNet structure under image size 64×64 was exactly the same as that in [8]. We extended this structure to the image size 128×128 in a similar way to the DCGAN, which is shown⁵ in Fig. 6. We adopted the spectral normalisation instead of the layer normalisation in the ResNet experiments and also encourage to refer to our implementations for more detail.

The FID and KID scores are given in Table 3, and the results of randomly generating, reconstructing and interpolating 128×128 images are provided in Fig. 7. More results on image sizes of 64×64 can be found in Fig. 8.

7.3 Proofs

7.3.1 Proof of Lemma 1

We here prove the non-negativity, symmetry and triangle properties that are required as a valid distance metric.

⁵Please note that the *critic* of our ResNet 128×128 structure is slightly different from that in the spectral GAN [9]. We adopted a symmetric (mirror) structure of the generator, whereby the spectral GAN used an asymmetric one. Although RCF-GAN still works under the structure of the spectral GAN, we believe that the mirror structure can well reflect the proposed reciprocal idea and is also a natural extension of the ResNet 64×64 in [8]. The parameter size in our ResNet structure is slightly smaller than that in the spectral GAN.



Figure 7: Random generation, reconstruction and interpolation by the proposed RCF-GAN by ResNet in terms of image size 128×128 . The upper panel shows images of the CelebA dataset and the lower panel is for the LSUN_B dataset.

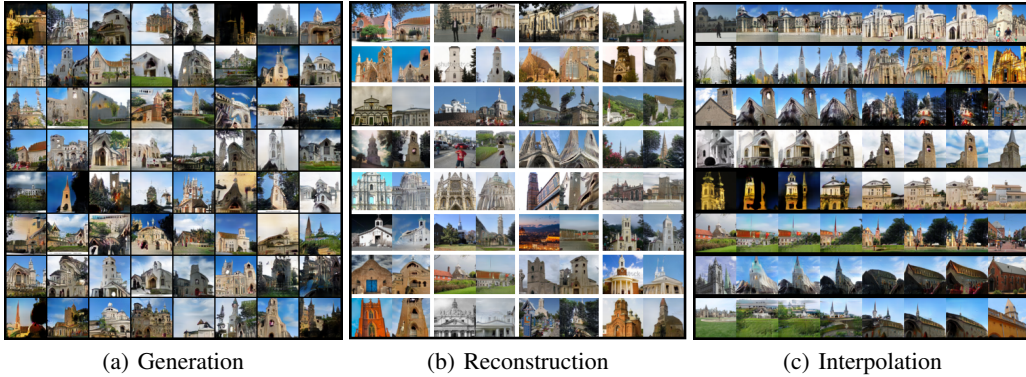


Figure 8: LSUN Church images generated, reconstructed and interpolated by the RCF-GAN by ResNet in terms of image size 64×64 . In this experiment, the employed ResNet was slightly different from the one in Fig. 6 by using the layer normalisation.

Non-negativity: Based on the definition of $\mathcal{C}_{\mathcal{T}}(\mathcal{X}, \mathcal{Y})$ in (4), the term $\mathcal{C}_{\mathcal{T}}(\mathcal{X}, \mathcal{Y})$ is non-negative because $c(\mathbf{t}) \geq 0$ for all \mathbf{t} . We next prove when the equality holds.

- $\mathcal{X} =^d \mathcal{Y} \rightarrow \mathcal{C}_{\mathcal{T}}(\mathcal{X}, \mathcal{Y}) = 0$: This is evident because $\Phi_{\mathcal{X}}(\mathbf{t}) = \Phi_{\mathcal{Y}}(\mathbf{t})$ for all \mathbf{t} .
- $\mathcal{X} =^d \mathcal{Y} \leftarrow \mathcal{C}_{\mathcal{T}}(\mathcal{X}, \mathcal{Y}) = 0$: Given that the support of \mathcal{T} is \mathbb{R}^m , $\int_{\mathbf{t}} \sqrt{c(\mathbf{t})} dF_{\mathcal{T}}(\mathbf{t}) = 0$ exists if and only if $c(\mathbf{t}) = 0$ everywhere. Therefore, $\Phi_{\mathcal{X}}(\mathbf{t}) = \Phi_{\mathcal{Y}}(\mathbf{t})$ for all $\mathbf{t} \in \mathbb{R}^m$. According to the *Uniqueness Theorem* of the CF, we have $\mathcal{X} =^d \mathcal{Y}$.

Therefore, $\mathcal{C}_{\mathcal{T}}(\mathcal{X}, \mathcal{Y}) \geq 0$, and the equality holds if and only if $\mathcal{X} =^d \mathcal{Y}$.

Symmetry: This is obvious for the symmetry of $c(\mathbf{t})$, thus yielding $\mathcal{C}_{\mathcal{T}}(\mathcal{X}, \mathcal{Y}) = \mathcal{C}_{\mathcal{T}}(\mathcal{Y}, \mathcal{X})$.

Triangle: Because the CFs $\Phi_{\mathcal{X}}(\mathbf{t})$ and $\Phi_{\mathcal{Z}}(\mathbf{t})$ are the elements of the normed vector space, we have the following inequality (also known as the Minkowski inequality),

$$\begin{aligned} & \int_{\mathbf{t}} |\Phi_{\mathcal{X}}(\mathbf{t}) - \Phi_{\mathcal{Z}}(\mathbf{t}) + \Phi_{\mathcal{Z}}(\mathbf{t}) - \Phi_{\mathcal{Y}}(\mathbf{t})| dF_{\mathcal{T}}(\mathbf{t}) \\ & \leq \int_{\mathbf{t}} |\Phi_{\mathcal{X}}(\mathbf{t}) - \Phi_{\mathcal{Z}}(\mathbf{t})| dF_{\mathcal{T}}(\mathbf{t}) + \int_{\mathbf{t}} |\Phi_{\mathcal{Z}}(\mathbf{t}) - \Phi_{\mathcal{Y}}(\mathbf{t})| dF_{\mathcal{T}}(\mathbf{t}). \end{aligned} \quad (9)$$

Therefore, the triangle property of $\mathcal{C}_{\mathcal{T}}(\mathcal{X}, \mathcal{Y})$ follows as

$$\mathcal{C}_{\mathcal{T}}(\mathcal{X}, \mathcal{Y}) \leq \mathcal{C}_{\mathcal{T}}(\mathcal{X}, \mathcal{Z}) + \mathcal{C}_{\mathcal{T}}(\mathcal{Z}, \mathcal{Y}). \quad (10)$$

This means that $\mathcal{C}_{\mathcal{T}}(\mathcal{X}, \mathcal{Y})$ is a valid distance metric in measuring discrepancies between two random variables \mathcal{X} and \mathcal{Y} .

This completes the proof.

7.3.2 Proof of Lemma 2

The proof of the triangle and symmetry properties is the same as those in Lemma 1. The non-negativity is also evident and the same as that in Lemma 1 but the equality holds for different conditions. We provide its proof in the following.

Before proceeding with the proof, we first quote Theorem 3 from Essen [47].

Theorem 3 ([47]) *The distributions of two random variables \mathcal{X} and \mathcal{Y} are the same when*

- $\Phi_{\mathcal{X}}(\mathbf{t}) = \Phi_{\mathcal{Y}}(\mathbf{t})$ in an interval around $\mathbf{0}$;
- $\beta_k = \int_{\mathcal{X}} x^k dF_{\mathcal{X}}(x) < \infty$ for $k = 0, 1, 2, 3, \dots$
- $\sum_{k=1}^{\infty} 1/\beta_{2k}^{1/2k}$ diverges, which means that the moment problem of β_k is determined and unique.

It is the fact that only requiring $\Phi_{\mathcal{X}}(\mathbf{t}) = \Phi_{\mathcal{Y}}(\mathbf{t})$ in an interval around $\mathbf{0}$ does not ensure the equivalence between two distributions without any other constraints, also given the counterexample provided in [47]. This equivalence cannot be ensured even when all the moments are matched. The third condition, intuitively, guarantees this equivalence by restricting that the moment does not increase “extremely” fast when $k \rightarrow \infty$.

In Lemma 2 of this work, we bound \mathcal{X} and \mathcal{Y} by $[-1, 1]$, thus having $|\beta_k| \leq 1 < \infty$ and $1/\beta_{2k}^{1/2k} \geq 1$ so that $\sum_{k=1}^{\infty} 1/\beta_{2k}^{1/2k}$ diverges. In this case, according to Theorem 3, we have $\Phi_{\mathcal{X}}(\mathbf{t}) = \Phi_{\mathcal{Y}}(\mathbf{t})$ when \mathbf{t} samples around $\mathbf{0} \rightarrow \mathcal{X} \stackrel{d}{=} \mathcal{Y}$. Conversely, it is obvious that $\mathcal{X} \stackrel{d}{=} \mathcal{Y} \rightarrow \Phi_{\mathcal{X}}(\mathbf{t}) = \Phi_{\mathcal{Y}}(\mathbf{t})$ for all \mathbf{t} . Therefore, as for bounded \mathcal{X} and \mathcal{Y} , sampling around $\mathbf{0}$ is sufficient to ensure the symmetry, triangle, non-negativity (together with the uniqueness when the equality holds) properties of $\mathcal{C}_{\mathcal{T}}(\mathcal{X}, \mathcal{Y})$.

This completes the proof.

7.3.3 Proof of Lemma 3

We first show the boundedness of $\mathcal{C}_{\mathcal{T}}(\mathcal{X}, \mathcal{Y})$ by observing

$$\begin{aligned} 0 \leq \mathcal{C}_{\mathcal{T}}(\mathcal{X}, \mathcal{Y}) &= \int_{\mathbf{t}} |\Phi_{\mathcal{X}}(\mathbf{t}) - \Phi_{\mathcal{Y}}(\mathbf{t})| dF_{\mathcal{T}}(\mathbf{t}) \\ &\leq \int_{\mathbf{t}} |\Phi_{\mathcal{X}}(\mathbf{t})| dF_{\mathcal{T}}(\mathbf{t}) + \int_{\mathbf{t}} |\Phi_{\mathcal{Y}}(\mathbf{t})| dF_{\mathcal{T}}(\mathbf{t}) \leq 1 + 1 = 2, \end{aligned} \quad (11)$$

where the second inequality is obtained via the Minkowski inequality and the third one by the fact that the maximal modulus of the CF is 1. It should be pointed out that this property is important and advantageous because in this way our cost is bounded automatically. Otherwise, we may need to bound $f \in \mathcal{F}$ to ensure an existence of the supremum of some IPMs (such as the dual form of the Wasserstein distance used in the W-GAN).

To prove the differentiable property, we first expand $c(\mathbf{t})$ in $\mathcal{C}_{\mathcal{T}}(\mathcal{X}, \mathcal{Y}) = \int_{\mathbf{t}} \sqrt{c(\mathbf{t})} dF_{\mathcal{T}}(\mathbf{t})$ as

$$\begin{aligned} c(\mathbf{t}) &= (\operatorname{Re}\{\Phi_{\mathcal{X}}(\mathbf{t})\} - \operatorname{Re}\{\Phi_{\mathcal{Y}}(\mathbf{t})\})^2 \\ &\quad - (\operatorname{Im}\{\Phi_{\mathcal{X}}(\mathbf{t})\} - \operatorname{Im}\{\Phi_{\mathcal{Y}}(\mathbf{t})\})^2, \end{aligned} \quad (12)$$

where $\operatorname{Re}\{\Phi_{\mathcal{X}}(\mathbf{t})\} = \mathbb{E}_{\mathcal{X}}[\cos(\mathbf{t}^T \mathbf{x})]$ denotes the real part of the CF and $\operatorname{Im}\{\Phi_{\mathcal{X}}(\mathbf{t})\} = \mathbb{E}_{\mathcal{X}}[\sin(\mathbf{t}^T \mathbf{x})]$ for its imaginary part. Therefore, by regarding $c(\mathbf{t})$ as a mapping $\mathbb{R}^m \rightarrow \mathbb{R}$, it is differentiable almost everywhere⁶.

This completes the proof.

⁶We note that $c(\mathbf{t})$ is not necessarily complex differentiable because it does not satisfy the Cauchy-Riemann equations. It is the fact that *nonconstant purely real-valued functions* are not complex differentiable because

7.3.4 Proof of Lemma 4

Because $\mathbb{E}_{\mathcal{Z}}[\|\mathbf{z} - f(g(\mathbf{z}))\|_2^2] = 0$ and $\|\mathbf{z} - f(g(\mathbf{z}))\|_2^2 \geq 0$, we have $\mathbf{z} = f(g(\mathbf{z}))$ for any \mathbf{z} and $g(\mathbf{z})$ under the supports of \mathcal{Z} and $\overline{\mathcal{Y}}$, respectively. We can obtain $g(\mathbf{z}) = g(f(g(\mathbf{z})))$ under the supports of \mathcal{Z} and $\overline{\mathcal{Y}}$ as well; given that $\overline{\mathbf{y}} = g(\mathbf{z})$ by the definition, this results in $\overline{\mathbf{y}} = g(f(\overline{\mathbf{y}}))$. Then, we have $\mathbb{E}_{\overline{\mathcal{Y}}}[\|\overline{\mathbf{y}} - g(f(\overline{\mathbf{y}}))\|_2^2] = 0$. Therefore, the function $g(\cdot)$ is a unique inverse of the function $f(\cdot)$, and vice versa, which also indicates that the two functions are bijective.

The bijection of the function $f(\cdot)$ possesses many desirable properties between the domains of $\overline{\mathcal{Y}}$ and \mathcal{Z} , thus ensuring the equivalences between their CFs. Specifically, without loss of generality, we assume $\mathcal{C}_{\mathcal{T}}(\overline{\mathcal{X}}, \overline{\mathcal{Y}}) = 0$, which means

$$\int_{\overline{\mathbf{x}}} e^{j\bar{\mathbf{t}}^T \overline{\mathbf{x}}} dF_{\overline{\mathcal{X}}}(\overline{\mathbf{x}}) = \int_{\overline{\mathbf{y}}} e^{j\bar{\mathbf{t}}^T \overline{\mathbf{y}}} dF_{\overline{\mathcal{Y}}}(\overline{\mathbf{y}}), \quad \text{for all } \bar{\mathbf{t}}. \quad (13)$$

Then, given the bijection $f(\cdot)$ by $\mathcal{X} = f(\overline{\mathcal{X}})$ and $\mathcal{Y} = f(\overline{\mathcal{Y}})$, we obtain $\mathbf{x} = f(\overline{\mathbf{x}}) = f(\overline{\mathbf{y}}) = \mathbf{y} \Leftrightarrow \overline{\mathbf{x}} = \overline{\mathbf{y}}$, for any realisations \mathbf{x} and \mathbf{y} from \mathcal{X} and \mathcal{Y} . We then have the following equivalence between the CFs of $\mathcal{X} = f(\overline{\mathcal{X}})$ and $\mathcal{Y} = f(\overline{\mathcal{Y}})$,

$$\begin{aligned} \int_{\overline{\mathbf{x}}} e^{j\bar{\mathbf{t}}^T \overline{\mathbf{x}}} dF_{\overline{\mathcal{X}}}(\overline{\mathbf{x}}) &= \int_{\overline{\mathbf{y}}} e^{j\bar{\mathbf{t}}^T \overline{\mathbf{y}}} dF_{\overline{\mathcal{Y}}}(\overline{\mathbf{y}}), \quad \text{for all } \bar{\mathbf{t}} \\ \Leftrightarrow \int_{\overline{\mathbf{x}}} e^{j\mathbf{t}^T f(\overline{\mathbf{x}})} dF_{\overline{\mathcal{X}}}(\overline{\mathbf{x}}) &= \int_{\overline{\mathbf{y}}} e^{j\mathbf{t}^T f(\overline{\mathbf{y}})} dF_{\overline{\mathcal{Y}}}(\overline{\mathbf{y}}), \quad \text{for all } \mathbf{t} \\ \Leftrightarrow \int_{\mathbf{x}} e^{j\mathbf{t}^T \mathbf{x}} dF_{\mathcal{X}}(\mathbf{x}) &= \int_{\mathbf{y}} e^{j\mathbf{t}^T \mathbf{y}} dF_{\mathcal{Y}}(\mathbf{y}), \quad \text{for all } \mathbf{t}. \end{aligned} \quad (14)$$

Therefore, we have $\mathcal{C}_{\mathcal{T}}(f(\overline{\mathcal{X}}), f(\overline{\mathcal{Y}})) = 0$. Furthermore, we also have $f(\overline{\mathcal{Y}}) \stackrel{d}{=} \mathcal{Z}$ due to $\mathbb{E}_{\mathcal{Z}}[\|\mathbf{z} - f(g(\mathbf{z}))\|_2^2] = 0$. Therefore, we have the following equivalences: $\mathcal{C}_{\mathcal{T}}(\overline{\mathcal{X}}, \overline{\mathcal{Y}}) = 0 \Leftrightarrow \mathcal{C}_{\mathcal{T}}(f(\overline{\mathcal{X}}), f(\overline{\mathcal{Y}})) = 0 \Leftrightarrow \mathcal{C}_{\mathcal{T}}(f(\overline{\mathcal{Y}}), \mathcal{Z}) = 0$ and $\mathcal{C}_{\mathcal{T}}(f(\overline{\mathcal{X}}), \mathcal{Z}) = 0$.

This completes the proof.

7.4 Related Works

IPM-GANs: Instead of the naive weight clipping in the W-GAN [5], the gradient penalty in W-GAN (W-GAN-GP) was proposed to mitigate the heavily constrained *critic* by penalising the gradient norm [8], followed by a further elegant treatment by restricting the largest singular value of the net weights [9]. It has been understood that although the *critic* cannot search within all satisfied Lipschitz functions [6, 7], the *critic* still performs as a way of transforming high dimensional but insufficiently supported data distributions into low dimensional yet broadly supported (simple) distributions in the embedded domain [14]. Comparing the embedded statistics, however, is much easier. For example, Cramer GAN compares the mean with an advanced \mathcal{F} from the Cramer distance to correct the biased gradient [49], whilst McGAN [11] explicitly compares the mean and the covariance in the embedded domain. Fisher GAN employs a scale-free Mahalanobis distance and thus a data dependent \mathcal{F} [10], which is basically the Fisher-Rao distance in the embedded domain between two Gaussian distributions with the same covariance. The recent Sphere GAN further compares higher-order moments up to a specified order, and avoids the Lipschitz condition by projecting onto a spherical surface [12]. Moreover, in a non-parametric way, BE-GAN directly employs an auto-encoder as the *critic*, whereby the auto-encoder loss was compared through embedded distributions [50]. The sliced Wasserstein distance has also been utilised into measure the discrepancy in the embedded domain [51]. Another non-parametric metric was achieved by the kernel trick of the MMD-GAN [13, 14], which treats \mathcal{F} as the reproducing kernel Hilbert space. However, one of the most powerful ways of representing a distribution, the CF, is still to be fully explored. More importantly, our RCF-GAN both directly compares the embedded distributions and also potentially generalises the MMD-GAN by flexible sampling priors.

Moreover, a very recent independent work [27] named OCF-GAN also employs the CF as a replacement by using the same structure of MMD-GANs. Our RCF-GAN is substantially different from that in [27]:

- Our *critic* operates as semantic embeddings and learns a meaningful embedded space, instead of being a component to build complete metrics as the existing GANs (e.g., OCF-GAN, MMD-GANs and W-GANs) do.
- Our CF design, is novel in its triangle anchor design with l_1 -norm (to stabilise convergence), meaningful analysis of amplitude and phase (to favour other distribution alignment tasks), t -net of outputting scales (to automatically optimise \mathcal{T} distribution types), and useful supporting theory (to correctly and efficiently use CF in practice).

their Cauchy-Riemann equations are not satisfied. However, in our case, it is differentiable as it is regarded as mappings in the real domain. Please refer to [48, 38] for more detail in the $\mathbb{C}\mathbb{R}$ calculus.

- Our RCF-GAN seamlessly combines the auto-encoder and GANs by using only two neat modules while achieving the state-of-the-art performances, whereas the majority of adversarial learning structures use at least three modules with auto-encoding separated from GANs.

Consequently, the results in [27] were reported given all images rescaled to the size of 32×32 , while our RCF-GAN consistently outperforms in various ways including high resolutions, net structures and functionalities.

Auto-encoders in an adversarial way: To address the smoothing artefact of the variational auto-encoder [41], several works aim to incorporate the adversarial style in (variational) auto-encoders, in the hope of gaining clear images whilst maintaining the ability of reconstruction. These mostly consist of at least three modules, an encoder, a decoder, and an adversarial modules [21–26]. To the best of our knowledge, there is one exception, called the adversarial generator encoder (AGE) [20], which incorporates two modules in adversarially training an auto-encoder under a *max-min* problem. The AGE still assumes the Gaussianity in the embedded distributions and only compares the mean and the diagonal covariance matrix; this is basically insufficient in identifying two distributions, and requires the pixel domain loss to be utilised supplementally in implementations. Our work, stilling playing a min-max problem, is fundamentally different from the AGE, as the auto-encoder in our RCF-GAN is a necessity to achieve the theoretical guarantee of a reciprocal, with the proposed anchor design. In contrast, without the auto-encoder, the AGE could still work by its Theorems 1 and 2 [20]. Furthermore, other than the first- and second-order moments, our work fully compares the discrepancies in the embedded domain via CFs. Benefiting from the powerful non-parametric metric via the CFs, our RCF-GAN only adversarially learns distributions in the embedded domain, that is, on a semantically meaningful manifold, without the need of any operation on the data domain.